HHS Public Access

Author manuscript

Neuroimage. Author manuscript; available in PMC 2023 February 27.

Published in final edited form as:

Neuroimage. 2022 November 01; 261: 119512. doi:10.1016/j.neuroimage.2022.119512.

Choroid plexus tissue perfusion and blood to CSF barrier function in rats measured with continuous arterial spin labeling

Hedok Lee[1,*], **Burhan Ozturk**[1], **Michael S. Stringer**[2], **Sunil Koundal**[1], **Bradley J. MacIntosh**[3], **Douglas Rothman**[4], **Helene Benveniste**[1]

[1]Department of Anesthesiology, Yale School of Medicine, New Haven, CT, USA

[2]Brain Research Imaging Centre and UK Dementia Research Institute, Centre for Clinical Brain Sciences, University of Edinburgh, Edinburgh, UK

[3]Department of Medical Biophysics, Faculty of Medicine, University of Toronto, Toronto, Canada.

[4]Departments of Radiology and Biomedical Imaging, Yale School of Medicine, New Haven, CT, USA

Abstract

The choroid plexus (ChP) of the cerebral ventricles is a source of cerebrospinal fluid (CSF) production and also plays a key role in immune surveillance at the level of blood-to-CSF-barrier (BCSFB). In this study, we quantify ChP blood perfusion and BCSFB mediated water exchange from arterial blood into ventricular CSF using non-invasive continuous arterial spin labelling magnetic resonance imaging (CASL-MRI). Systemic administration of anti-diuretic hormone (vasopressin) was used to validate BCSFB water flow as a metric of choroidal CSF secretory function. To further investigate the coupling between ChP blood perfusion and BCSFB water flow, we characterized the effects of two anesthetic regimens known to have large-scale differential effects on cerebral blood flow. For quantification of ChP blood perfusion a multi-compartment perfusion model was employed, and we discovered that partial volume correction improved measurement accuracy. Vasopressin significantly reduced both ChP blood perfusion and BCSFB water flow. ChP blood perfusion was significantly higher with pure isoflurane anesthesia (2-2.5%) when compared to a balanced anesthesia with dexmedetomidine and low-dose isoflurane (1.0 %), and significant correlation between ChP blood perfusion and BCSFB water flow was observed, however there was no significant difference in BCSFB water flow. In summary, here we introduce a non-invasive, robust, and spatially resolved in vivo imaging platform to quantify ChP blood perfusion as well as BCSFB water flow which can be applied to study coupling of these two key parameters in future clinical translational studies.

[*]**Corresponding author:** Hedok Lee, PhD, Department of Anesthesiology, 89 Howard Avenue, Fl 3rd, Rm 432, New Haven, CT, 06519, USA, hedok.lee@yale.edu, Telephone: 201-421-7315.

Data and declaration of conflicting interests

The author(s) declared no potential conflicts of interest with respect to the research, authorship, and/or publication of this article.

Supplementary materials

Supplemental materials for this article are available online.

Credit authorship contribution statement

Hedok Lee: Conceptualization, Methodology, Software, Investigation, Writing. Burhan Ozturk : Methodology, Investigation. Michael Stringer: Conceptualization, Writing. Sunil Koundal: Investigation. Bradley MacIntosh: Conceptualization, Writing. Douglas Rothman: Methodology, Writing. Helene Benveniste: Conceptualization, Methodology, Supervision, Funding acquisition, Writing.

1. Introduction

The glymphatic system for brain waste disposal was discovered a decade ago (Benveniste et al., 2019; Iliff et al., 2012; Jessen et al., 2015; Tarasoff-Conway et al., 2015; Wardlaw et al., 2020). According to the glymphatic system model, CSF flows into peri-arterial Virchow-Robin channels and exchanges with interstitial fluid (ISF) in a manner dependent on astroglial aquaporin-4 water channels. The CSF-ISF 'mixing' propels waste, including amyloid beta (Aβ) and tau, towards egress routes which ultimately coalesce with authentic lymphatic vessels and the systemic circulation. Glymphatic system function and waste clearance is critically dependent on central nervous system (CNS) fluid homeostasis, including the ability to produce and reabsorb CSF at a sustainable and physiologically normal rate. The stable milieu of brain interstitial fluid constitutes the essence of CNS fluid homeostasis in the healthy brain (Benveniste et al., 2019; Louveau et al., 2017). Accordingly, because glymphatic function requires CSF exchange with interstitial fluid for waste clearance, the physiological balance of CSF production and reabsorption is critical for overall fluid homeostasis. Dysregulation of CSF homeostasis i.e., CSF production and reabsorption can occur in several conditions including trauma to the dura mater causing CSF leakage, or with different types of hydrocephalus and these conditions are associated with decreased glymphatic system transport (Benveniste et al., 2020; Plog et al., 2019). It is generally assumed that 80% of CSF is continuously secreted by the choroid plexuses (ChP) (Praetorius et al., 2020) known as 'blood to CSF barrier' (BCSFB) but there is a gap in knowledge of how changes in CSF production impact glymphatic waste clearance and neurodegenerative processes such as Alzheimer's disease. This lack of information is linked to the technical challenges involved in quantifying CSF production non-invasively. For decades ChP secretory function has been quantified in dogs, sheep, and mice using the tracer dilution method which is invasive and also associated with inaccuracies (Heisey et al., 1962; Oreskovic et al., 2017). More recently an alternative invasive technique was developed which directly tracks CSF secretion from the ventricles in rats (Karimy et al., 2015; Karimy et al., 2017). This technique recently confirmed that the CSF secretion rate in rodents depended on aging and also provided new information on the effect of various anesthetics (Liu et al., 2020). Notably, all of these methods are invasive and limits translational studies of CSF secretion in human subjects, therefore there is a great need for novel non-invasive techniques.

Recently, a non-invasive approach was introduced to quantify BCSFB mediated delivery of arterial blood water from the ChP into ventricular CSF using arterial spin labelling magnetic resonance imaging (BCSFB-ASL) in mice (Evans et al., 2020; Perera et al., 2021). Arterial spin labelling (ASL) is a non-invasive magnetic resonance imaging technique used to quantify cerebral blood flow by using magnetically labeled inflowing arterial blood water as an endogenous tracer (Alsop et al., 2015; Grade et al., 2015; Telischak et al., 2015; Williams et al., 1992), which is increasingly used in clinical research studies of cerebral small vessel diseases, stroke, and other neurological disorders (Cada et al., 2000; De Jong et al., 1999; Ho, 2018; Iturria-Medina et al., 2016). The novel BCSFB-ASL imaging approach was previously validated in mice by demonstrating that administration of anti-diuretic hormone vasopressin downregulated BCSFB secretory function (Evans et al.,

2020). Vasopressin – also called anti-diuretic hormone - interacts with at least 2 types of receptors, V1 and V2, and influence brain water homeostasis via V1 receptors expressed by choroid plexus. Vasopressin acts by reducing ChP blood perfusion in a dose dependent manner via V1 receptors expressed in the smooth muscle cells of choroidal blood vessels causing vasoconstriction and increased vascular resistance (Brinton et al., 1984; Faraci et al., 1988; Fernandez et al., 2001; Phillips et al., 1988; Vakili et al., 2005). Another study reported that vasopressin administered as a continuous intravenous infusion reduced ChP perfusion as well as the CSF secretion implying that ChP perfusion and CSF secretory function are tightly coupled (Faraci et al., 1994).

Although the new non-invasive BCSFB-ASL based approach may indeed track BCSFB secretory function, the signal to noise ratio (SNR) in ASL acquisitions is inherently poor and the BCSFB-ASL protocol requires data acquisition at long echo time (TE) that makes it even more challenging to acquire high quality and robust data. Further, quantification of blood perfusion of the ChP tissue is an important metric to also measure for full interpretation of how the coupling of ChP perfusion and secretory function changes in disease and with pharmacological manipulation. In this study we addressed these challenges by implementing a continuous ASL (CASL) sequence at 9.4 T and by applying a multi-compartment perfusion model to quantify ChP tissue perfusion as well as BCSFB water flow in rats.

2. Materials and methods

2.1 Animals

The animal experiments were approved by the local Institutional Animal Care and Use Committee at Yale University (New Haven, Connecticut) and conducted in accordance with the United States Public Health Service's Policy on Humane Care. Twelve female Wistar Kyoto (WKY) rats (Charles River Laboratories, Wilmington, MA, USA) between the ages of 9 month (M) to 12M were used. All rats received standard rat chow and water ad libitum and were housed in standard conditions in a 12h light/dark cycle.

2.2 Anesthesia and preparation for MRI

Prior to commencing MRI acquisitions, rats underwent anesthesia induction using 3% isoflurane (ISO) delivered in 100% oxygen (O_2). The anesthetized rats were placed in a custom 3D printed rat body holder in prone position while breathing spontaneously through a snout mask (see Supplementary Material 1). For rats undergoing MRI with pure ISO (N=12), the anesthesia was maintained with 2-2.5% ISO throughout the experiments. For rats undergoing MRI under balanced anesthesia with dexmedetomidine supplemented with 1% ISO (DEXM-I) regimen (N=12), a bolus of dexmedetomidine (0.007mg/kg i.p.) was given after ISO induction and followed by continuous infusion of dexmedetomidine at a rate of 0.009 ± 0.002mg/kg/h administered via a subcutaneous catheter. In both ISO and DEXM-I experiments, ISO was delivered in a 1:1 Air:O_2 mixture as described previously (Benveniste et al., 2017; Ozturk et al., 2021). During MRI session (protocol described below), the respiratory rate, heart rate, and body temperature were measured continuously by non-invasive MRI compatible monitors (SA Instruments, Stony Brook, NY, USA).

Body temperature was maintained between 36.5–37.5°C using a heated waterbed system. Following completion of MRI scanning, the rats were recovered from anesthesia in their home cage and were observed until they regained normal behavior.

2.3 MRI acquisition

MRI was performed on a Bruker 9.4T/16 magnet (Bruker BioSpin, MA, USA), operating with Paravision 6.0.1 software, and interfaced with an Avance III-HD console. A custom-made transverse electromagnetic resonator style transmit-receive radiofrequency (RF) coil (Bolinger et al., 1989) with an internal diameter of 50mm with active decoupling was used for imaging (see Supplementary Material 1). Flowchart for the MR data acquisitions and analysis pipelines implemented in different experiments is shown in Fig .1.

Anatomical T2 weighted MRI: To ensure accurate and reliable positioning of the imaging slice for the CASL (see Supplementary Material 1), two-dimensional (2D) T2-weighted (T2W) anatomical brain images were obtained in sagittal and axial orientations using a RARE sequence with the following parameters: repetition time (TR) = 2500ms, echo time (TE) = 22ms, number of acquisitions (NA) = 1, RARE factor = 4, in plane resolution = 0.23mm/voxel, slice thickness = 1.0mm.

Continuous arterial spin labeling: A 2D single-slice CASL sequence was performed using a single-shot spin echo EPI. Anterior commissure was identified on the anatomical T2W image and used as an anatomical reference for ensuring the inclusion of choroid plexus within the field of view; correct image plane for CASL (see Supplementary Material 1). Cortical blood perfusion (CTX), apparent ChP blood perfusion, ChP tissue perfusion and BCSFB mediated water exchange termed ‘BCSFB water flow’ were measured by incorporating a short TE followed by a long TE CASL-based acquisition. The short TE CASL sequence was performed with 9 post labelling delays (PLD = 10, 100, 200, 400, 700, 1100, 1500, 2000, 3000ms) using the following parameters: TR = 7000ms, TE = 23ms, NA = 20, acquisition matrix = 64 x 64, in plane resolution = 0.45mm/voxel, slice thickness = 1.0mm, labelling duration (LD) = 3000ms, scanning time 4min 40sec per PLD. Similarly, for the long TE CASL, the CASL sequence was performed at 9 post labelling delays (PLD = 10, 200, 400, 700, 1100, 1500, 2000, 3000, 4000ms) using following parameters: TR = 11000ms, TE=150ms, NA = 20, acquisition matrix = 64 x 64, in plane resolution = 0.45mm/voxel, slice thickness = 1.0mm, LD = 6000ms, scanning time 7min 20sec per PLD. A proton density weighted image, M_0, was acquired by collecting control images with the following parameters: TR = 20000ms, TE = 23 and 150ms, NA = 4, scanning time 1min 20sec. A hard pulse was used for a flow-driven adiabatic inversion at 23 ± 2mm distal to the imaging plane using a separate single-turn actively decoupled arterial blood labeling coil, minimizing the magnetization transfer effect during the labeling period (see Supplementary Material 1). In both the labeling and control image acquisitions, a 10mT/m labelling gradient was applied along the z direction. RF power of the labelling coil was set to 6 μT (Zhang et al., 1993). Control and labeled images were acquired in an interleaved fashion and pair-wise subtraction, $\Delta M = M_{control} - M_{labeled}$, was calculated to derive the perfusion weighted image (PWI).

T1 relaxometry: A 2D inversion recovery sequence was performed to calculate the tissue longitudinal relaxation time (T1) needed for perfusion measurements. A single shot and single slice echo planar imaging (EPI) imaging sequence was acquired with the same image position and spatial resolution as the CASL with the following parameters: TR = 15000ms, TE = 23ms, NA = 1, 25 inversion times ranging from 100-9000ms, acquisition matrix = 64 x 64, in plane resolution = 0.45mm/voxel, slice thickness = 1.0mm, scanning time 6min 15s.

T2 relaxometry: A 2D multi-spin multi-echo (MSME) sequence was performed to derive T2 distribution curves for calculating tissue and CSF partial volumes. A single slice MSME sequence was acquired with the same image position and spatial resolution as the CASL and 80 evenly spaced TEs were performed with the following parameters: TR = 6000ms, TE = 10-800ms, ΔTE = 10ms, NA = 1, acquisition matrix = 64 x 64, in plane resolution = 0.45mm/voxel, slice thickness = 1.0mm, scanning time 6min 24sec.

B1+ mapping: Since the accuracy of T2 multi-compartment relaxometry is sensitive to the spatially varying RF transmit (B1+) homogeneity, B1+ maps were acquired in a subset (N = 9) of the rats using a double angle method as described previously (Lee et al., 2018; Stollberger and Wach, 1996). 2D RARE sequence was performed at two flip angles in the same position and spatial resolution as the CASL using following parameters: TR = 10000ms, TE = 22ms, NA = 20 , FA = 70° and 140°, RARE factor = 4, acquisition matrix = 64 x 64, in plane resolution = 0.45mm/voxel, slice thickness = 1.0mm, scanning time 11min.

2.4 MRI analyses

T1 relaxometry: Voxel-wise T1 calculations were performed by fitting image intensities of the inversion recovery sequence as a function of inversion times expressed in eq. 1 as:

$$S_{T1} = S_0\left[1 - (1 - cos\theta)e^{-TI/T1} - cos\theta e^{-TR/T1}\right], \quad [1]$$

where S_{T1}, S_0, θ, TI, and $T1$ represent image intensity, proton-density weighted signal, flip angle, inversion time, and longitudinal relaxation time, respectively. The three unknown variables (S_0, θ, and $T1$) were calculated by the Nelder-Mead Simplex non-linear least square fitting algorithm as described previously (Lee et al., 2018).

Multi compartment T2 relaxometry: Multi compartment T2 relaxometry analysis was performed to identify distinct compartments through the smooth T2 distribution curves formulated as a linear combination of exponential functions expressed in eq. 2 as

$$S_{MSME} = \int_{T2\,\min}^{T2\,\max} S(T_2)e^{-TE/T_2}dT_2 + \beta, \quad [2]$$

where $S(T_2)$ is the fractional contribution of a given T2 to the overall signal S_{MSME} and β is a signal offset (Does, 2018; Kroeker and Henkelman, 1986; Provencher, 1982a). S_{MSME} is defined as the mean image intensities derived from the MSME sequence within the regions of interest (CTX and ChP). The CONTIN decomposition technique (Provencher, 1982b) applies a regularized Laplace inversion and solves for an appropriate set of smooth

continuous T2 distribution curve, $S(T_2)$, within the lower ($T2_{min} = 10ms$) and upper ($T2_{max} = 1000ms$) limits as a solution to the eq.2 (Marino, 2021; Provencher, 1982a). dT_2 was discretized by 40 bins spaced logarithmically from $T2_{min}$ to $T2_{max}$. Following the calculation of a T2 distribution curve, $S(T_2)$ was further divided into tissue and CSF compartments whose T2 ranges were characterized by short T2 ($10ms < S(T_2) \leq 100ms$) in tissue and long T2 ($100ms < S(T_2) \leq 1000ms$) in CSF and the areas under the distribution curves within the limits defined the fractional contribution of the tissue (P_{tissue}) and CSF (P_{CSF}) compartments. An expectation value, $E[T_2]$, whose probability density function was defined by the T2 distribution curve, was calculated to identify the peak of T2 within the range of each compartment. Overview of the procedure implemented for calculating the fractional contributions and the expectation values is shown in the Supplementary Material 2.

Evaluation of CONTIN algorithm using computer simulations: The accuracy of the CONTIN decomposition technique for calculating the T2 distribution curve was evaluated using computer simulations incorporating a broad range of measurement conditions. MSME image intensity, $S_{simulated}$, was simulated by a bi-exponential function expressed in eq. 3 as

$$S_{simulated} = S_{0s}\left((1 - P_{CSF})\, e^{-TE/T21} + P_{CSF} e^{-TE/T22}\right) + N(0,1), \quad [3]$$

where S_{0s}, $T21$, $T22$, *and* $N(0,1)$ represent the simulated water proton signal, T2 of tissue at 40ms, T2 of CSF at 300ms, and a noise term defined by a normal distribution with a fixed mean (0) and standard deviation (1), respectively. $S_{simulated}$ was calculated at 80 evenly spaced TEs from 10ms to 800ms and S_{0s} was set to 60, 100, and 200 in simulating various SNR conditions. A total of 5000 trials was performed for a given set of variables (S_{0s}, $0.1 \leq P_{CSF} \leq 0.9$) and $E[T_{21}]$, $E[T_{22}]$, and P_{CSF} were calculated at each trial. Discrepancy between the calculated and the given set of values (T_{21} = 40ms T_{22} = 300ms and P_{CSF} = 0.1 - 0.9) were quantified and expressed in eq. 4 as

$$discrepency = \left(\frac{V_{CONTIN} - V_{given\text{-}value}}{V_{given\text{-}value}}\right) 100\,\%, \quad [4]$$

where V_{CONTIN} and $V_{given\text{-}value}$, represent the calculated and corresponding given values in $E[T_{21}]$, $E[T_{22}]$, and P_{CSF}, respectably.

Manual delineations of regions of interest: ChP and somatosensory CTX were manually delineated as shown in Fig .2 (also see Supplementary Material 3). Perfusion weighted images taken at TE = 23ms, $\Delta M_{TE=23ms}$, were summed over all PLDs and used as a template for identifying the CTX. Similarly, at the level of the ChP, the BCSFB weighted images acquired at TE=150ms, $\Delta M_{TE=150ms}$, were summed over all PLDs and the conspicuous regions within the lateral ventricles were delineated. A publicly available free software MRICron (https://www.nitrc.org/projects/mricron) was utilized for the manual delineations.

Cortical perfusion, apparent ChP perfusion, and BCSFB water flow measured by CASL: In the short TE CASL measurement, the coarse spatial resolution of the CASL sequence relative to the size of the ChP manifests as signal mixing between the ChP tissue perfusion (f_{ChP}) and the BCSFB water flow (f_{BCSFB}), analogous to the partial volume effect between different tissue compartments (Asllani et al., 2008; Chappell et al., 2018; Chappell et al., 2021). The signal mixing resulting in apparent ChP blood perfusion, $f_{ChP\text{-}BCSFB}$, was modeled as the sum of the partial contributions of f_{ChP} and f_{BCSFB} expressed in eq. 5 as

$$f_{ChP\text{-}BCSFB} = (1 - P_{CSF}) f_{ChP} + P_{CSF} f_{BCSFB}, \quad [5]$$

where $f_{ChP\text{-}BCSFB}$ and f_{BCSFB} were calculated directly from the CASL measurements taken at short TE and long TE CASL, respectively, as expressed in eq. 6 and P_{CSF} was calculated from the T2 relaxometry. We expressed $f_{ChP\text{-}BCSFB}$ as a linear combination of the ChP tissue perfusion and BCSFB water flow as the (single) compartmental origin of the signal captured at $f_{ChP\text{-}BCSFB}$. In the model we also assumed instantaneous exchange of labelled water from blood to tissue and from blood to CSF and did not implement the dynamic exchange between the ChP tissue perfusion and BCSFB water flow in the model. Overview of the experiment is also shown in Fig.1A.

The calculations of CTX blood perfusion (f_{CTX}), apparent ChP blood perfusion ($f_{ChP\text{-}BCSFB}$), and BCSFB water flow (f_{BCSFB}) were performed by implementing a standard single compartment model (Alsop et al., 2015; Buxton et al., 1998), where f_{CTX} and f_{BCSFB} represent the rate of labelled arterial blood water exchanging with tissue and CSF, respectively. In the single compartment model, the relationship between the pair-wise subtraction, $\Delta M = M_{control} - M_{labeled}$, and f_{CTX} and f_{BCSFB} was expressed by

$$\Delta M = \begin{cases} 0 & 0 < t < ATT \\ 2M_{0b} f T_{1a} \alpha e^{-\frac{ATT}{T1_b}} (1 - e^{-\frac{t-ATT}{T1_a}}) & ATT < t < \tau + ATT \\ 2M_{0b} f T_{1a} \alpha e^{-\frac{ATT}{T1_b}} e^{-\frac{t-\tau-ATT}{T1_a}} (1 - e^{-\frac{\tau}{T1_a}}) & \tau + ATT < t \end{cases}, \quad [6]$$

where, f, T_{1b}, α, ATT, and τ represent the tissue perfusion (or BCSFB water flow) given in the units of ml/min/100g, T1 of blood assumed to be 2400ms, the arterial blood inversion efficiency assumed to be 0.8, the arterial transit time, and the arterial blood labeling duration, respectively (Dobre et al., 2007; Hirschler et al., 2020). Note that t is the time measured from the start of the arterial blood water labeling to the time of the image acquisition ($LD+PLD$). f and ATT, in eq. 6, were solved by fitting $\Delta M/M_{0b}$ as a function of PLDs using the Levenberg–Marquardt non-linear least square algorithm written in-house MATLAB code (MathWorks, Natick, MA, USA). Initial conditions of f and ATT were set to 200 and 500ms, respectively, and the parameter search range was constrained within following limits: 10ml/100g/min ≤ f ≤ 500ml/100g/min and 10ms ≤ ATT ≤ 3000ms (Larkin et al., 2019; Thomas et al., 2006). f_{CTX} and $f_{ChP\text{-}BCSFB}$ were calculated by using the CASL sequence acquired at TE = 23ms ($\Delta M_{TE=23\,ms}$) and f_{BCSFB} was calculated by using the CASL sequence acquired at TE = 150ms ($\Delta M_{TE=150\,ms}$). M_{0b} in both f_{CTX} and $f_{ChP\text{-}BCSFB}$ represents the equilibrium magnetization of arterial blood which was approximated by the

equilibrium magnetization of tissue, $M_{0\text{-}TE=23ms}$, derived from the image acquired at TR = 20000ms and TE = 23 ms which was then divided by the water tissue to blood partition coefficient, assumed to be 0.98 in f_{CTX} and 1.05 in $f_{ChP\text{-}BCSFB}$ (Chappell et al., 2018; Herscovitch and Raichle, 1985). T_{1a} in f_{CTX} and $f_{ChP\text{-}BCSFB}$ was approximated by an apparent T1 of CTX and ChP measured by the inversion recovery T1 mapping technique taken at TE = 23ms. In $f_{BCSFB,}$ M_{0b} was approximated by the equilibrium magnetization of CSF, $M_{0\text{-}CSF}$, however $M_{0\text{-}CSF}$ cannot be directly measured since the ROI of ChP comprises partial volume effect of ChP tissue and CSF, therefore $M_{0\text{-}CSF}$ was estimated by using the linear regression algorithm which extrapolated the image intensity of ChP taken at TR = 20000ms and TE = 150ms, $M_{0\text{-}TE=150ms}$, at the limit of pure CSF (see Supplementary Material 4) (Asllani et al., 2008; Parkes et al., 2004).

Effects of vasopressin on ChP blood perfusion and BCSFB water flow: To characterize the effects of the anti-diuretic hormone vasopressin, a subset of female WKY rats (N=8) were used. Following anesthesia with 2-3% ISO delivered in 100% oxygen and with the rats breathing spontaneously, a PE-50 femoral infusion line was placed for intravenous administration of vasopressin (Vasostrict Par Pharmaceutical Companies, USA). The rats were subsequently transported to the MRI scanner with the intravenous femoral infusion line long enough to continuously infuse vasopressin from the outside of the scanner using a micro-infusion pump (Legato 130 syringe pump, KD Scientific, USA). During imaging the rats were anesthetized with 2-3% ISO delivered with a 1:1 Air:O_2 mixture and breathing spontaneously. The pharmacological MRI (ph-MRI) protocol comprised short (23ms) and long (150ms) TE CASL at a fixed PLD acquired in an interleaved manner (Perera et al., 2021) using the following parameters TR = 11000ms, TE = 23/150ms, number of acquisitions (NA) = 10/20, acquisition matrix = 64 x 64, in plane resolution = 0.45mm/voxel, slice thickness = 1.0mm, LD = 6000ms, PLD = 500/2000ms. Following baseline scans, comprising three blocks of short and long TE scans, a continuous infusion of vasopressin was commenced at a rate of 2mU/Kg/min (Faraci et al., 1990). Post-administration scans included a total of six blocks of short and long TE CASL scans lasting for 60minutes. Semi-quantitative image analysis was performed by calculating the % signal change between the average of the three baseline scans and the post administration scans. Overview of the experiment is also shown in Fig.1B.

Effects of anesthesia on ChP perfusion and BCSFB water flow: The modulatory effect of the two anesthetics regimens (DEXM-I and ISO) on f_{CTX}, f_{ChP}, $f_{ChP\text{-}BCSFB}$, and f_{BCSFB}, were carried out using a crossover repeated measures study design as described previously (Ozturk et al., 2021). All rats (N = 12) underwent two MRI scanning sessions in which the rats were randomly selected to undergo either DEXM-I or ISO in the first scanning session. Before the second scanning session, at least 7 days of rest was allowed to ensure wash-out effects of each anesthetic. In the second session, all rats underwent either DEXM-I or ISO so that all rats received both anesthetics over the two scanning sessions totaling 24 imaging sessions. The data are presented as mean estimates for the CASL outcomes with standard deviation (sd). For experiments with repeated measurements on each animal, pairwise comparisons were investigated using Wilcoxon signed-rank 2-sided test. Analyses were performed using the SPSS (New York, USA) statistical software

package and a p-value less than 0.05 was considered significant. Linear regression analyses were performed between the apparent ChP blood perfusion and ChP tissue perfusion with respect to BCSFB water flow using XLSTAT statistical data analysis software (New York, USA)

3. Results

3.1 TE-dependent perfusion weighted signal decay

Flowchart for the TE-dependent perfusion weighted signal decay is shown in Fig.1C and representative perfusion weighted images, ΔM, are shown in Fig.2A as a function of TEs. As seen from the figure, the signal from the brain tissue reached background noise levels around TE = 150ms, however, the signals within the lateral ventricles (LV), remained conspicuous even at TE = 200ms, implying an inherently longer T2 relaxation time compared to the brain tissue. Notably, the spatial distribution of ΔM image intensity within the LV was heterogenous as can be observed in Fig.2C (also see Supplementary Material 3). Specifically, while ΔM 'hot spots' were observed in the center of the LV, higher signals were associated with the ChP itself. Therefore, the source of hot spot regions in the center of the LV taken at TE =150ms or longer is BCSFB mediated water exchange in the CSF compartment of ChP.

Perfusion weighted signals in the CTX and ChP were calculated and plotted as a function of TEs (Fig.2D). Consistent with the observations in Fig.2A, CTX signals decayed considerably faster than ChP signals and in the CTX the mono-exponential characterization of ΔM fitted well even at the long TEs (red solid line, Fig.2D). In contrast, the mono-exponential curve fitted the ChP poorly in the end portion of the curve (TE = 100ms or greater), implying the existence of multiple compartments in the region of interest.

3.2 Evaluation of the CONTIN algorithm by computer simulations

The accuracy of the CONTIN algorithm for calculating T2 distribution curves in the simulated bi-exponential model, as expressed in eq.3, was evaluated by computer simulation modeling. At each trial, simulated bi-exponential data was analyzed by the CONTIN algorithm and a calculated T2 distribution curve was analyzed to derive, $E[T_{21}]$, $E[T_{22}]$, and P_{CSF} and compared with the given values (T_{21} = 40ms T_{22} = 300ms and P_{CSF} = 0.1 - 0.9). In Fig.3A averaged T2 distribution curves of all 5000 trials with P_{CSF} = 0.6 are shown at three different SNRs: 60, 100, 200. As expected, bimodal T2 distribution curves with two peaks at 40ms and 300ms were discernable. Line broadening around the peaks is caused by the noise in the simulations and becomes more pronounced with decreasing SNR but the broadening did not cause the peaks to overlap, and two peaks remained easily distinguishable. Discrepancies between the calculated and the given values $E[T_{21}]$, $E[T_{22}]$ and P_{CSF} are shown in the Fig.3B-D. Notably, with increasing SNR the accuracy improved in all of the three variables as expected and the accuracy of the calculated variables are dependent on the given fractional contribution, P_{CSF}. With increasing P_{CSF}, the peak at T_{22} = 300ms appeared more distinct, improving the detectability and reducing the discrepancies in calculating T_{22} and P_{CSF}. Conversely with decreasing P_{CSF}, the discrepancies in calculating the variables amplified.

3.3 T2 relaxometry in choroid plexus and cortex in rats

For each animal, the mean image intensities within the ROIs were calculated over all TEs and the population averaged mean intensities are plotted in Fig.3F along with the corresponding representataive images (Fig.3E). Similar to the trend observed in the perfusion weighted images (Fig.2D), the spin-echo image intensities also decayed more rapidly in CTX than ChP and reached background noise levels around TE = 150ms while the intensities associated with the ChP decayed more gradually and retained signal above the noise level even at TE = 800ms. At TE = 10ms, the SNR of the ChP was 103 ± 7 and the SNR of the CTX was 91 ± 6, derived by using a canonical form for calculating SNR (Firbank et al., 1999). Population averaged T2 distribution curves are also shown in Fig.3G. The T2 distribution curve in CTX manifested a unimodal distribution curve peaking at $E[T_{21}]$ = 38 ± 1ms implying a single compartment. In contrast, a bimodal distribution curve was observed within the ROI of the ChP with short and long T2 peaks at $E[T_{21}]$ = 41 ± 4ms and $E[T_{22}]$ = 301 ± 16ms, respectively. Coarse MR image resolution relative to the size of ChP, as shown in Fig.2C (also see Supplementary Material 3), inevitably results in partial volumes across ChP tissue and the surrounding CSF and the fractional contribution of CSF compartment, P_{CSF}, was 0.57 ± 0.08. Finally, the RF transmit inhomogeneity (B1+) was also analyzed within the ROI of ChP as it can significantly result in stimulated echoes corrupting the measured MSME signals (Prasloski et al., 2012). Nine rats underwent B1+ mapping using the double angle method (Stollberger and Wach, 1996) and yielded 0.953 ± 0.012 indicative of a highly homogeneous B1+ profile owing to the use of the volume transmit coil along with the ChP being positioned near the center of the coil.

3.4 Vasopressin MRI

Pharmacodynamics of the anti-diuretic hormone vasopressin was characterized through the interleaved CASL sequence acquired at short (23ms) and long (150ms) TEs with fixed PLDs. Representative time averaged (3 frames) perfusion and BCSFB weighted images are shown in Fig.4A. Notably, the perfusion weighted image intensities appear to increase progressively in the CTX after administration of vasopressin. In contrast, both the apparent ChP perfusion and the BCSFB weighted image intensities decreased progressively over time with vasopressin administration. Semi-quantitative characterization of the effect of vasopressin was assessed by calculating % signal change between the pre-(baseline) and post-vasopressin data for all animals and the results are plotted in Fig.4B. As seen from the representative images, the perfusion in CTX gradually increased during vasopressin administration and stabilized ~25% above the baseline after 60min, while both the apparent perfusion and BCSFB weighted signals of the ChP gradually decreased over time, reaching ~25% below the baseline at 60min. In spite of the progressive decrease of the BCSFB weighted signals over time, implying downregulation of BCSFB water flow, the volume of the lateral ventricles neither shrunk nor expanded as shown in Fig.4A (also see Supplementary Material 5).

3.5 Effects of anesthesia on choroid plexus perfusion and BCSFB water flow

Normalized ChP perfusion and BCSFB weighted signals, ($\Delta M/M_{0b}$), were fitted using the single compartment model expressed in eq.6 for deriving CTX blood perfusion, the apparent

ChP blood perfusion, and BCSFB water flow and the results are shown in Fig.5A-C and summarized in Table.1. Flowchart for the data acquisitions and analysis pipelines is shown in Fig.1A. $\Delta M/M_{0b}$ in all the animals (N = 12) are plotted as dots along with the group mean ± sd and the solid lines represent the corresponding model fitting using the population averaged f and ATT plotted separately for the two anesthetic regimens of DEXM-I and ISO.

As summarized in Table.1 and the ladder plots in Fig.5D-F ChP tissue perfusion was two to three folds higher than the CTX perfusion and the BCSFB water flow was only 25% of the ChP tissue perfusion values. The duration for the arterial blood to flow from the labeling region to the tissue, ATT, was also significantly longer in the apparent ChP perfusion compared to CTX irrespective of the anesthetic regimen. In addition, the duration for the arterial blood to arrive at the CSF through the BCSFB water flow was nearly doubled compared to that of the CTX perfusion. A Wilcoxon signed-rank 2-sided test was performed to compare the effect of the two anesthetics and yielded significant differences in the apparent ChP perfusion, ChP tissue perfusion, and CTX perfusion. ATTs were also significantly lower with ISO compared to DEXM-I in the apparent ChP perfusion and CTX perfusion likely due to the vasodilatory effect of ISO, elevating blood flow, thereby shortening the duration for the arterial blood to flow from the labeling region to reach the tissue (Wegener et al., 2007). Spatially resolved post labelling delay (PLD) summed perfusion and BCSFB weighted images are shown in Fig.6A and 6B. Reduced brain tissue perfusion with DEXM-I anesthesia compared to ISO is strikingly noticeable. As for the BCSFB weighted images, prominent signals of labelled blood water exchanging with CSF in the LV are conspicuous but differences between the two distinct anesthetic regimens are not discernable and statistical analyses of BCSFB water flow between the two anesthetics yielded a 13% reduction with DEXM-I compared to ISO but was not statistically significant (p-value = 0.077). Linear regression analysis revealed significant correlations between the apparent ChP perfusion and BCSFB water flow (p-value = 0.012) and between ChP tissue perfusion and BCSFB water flow (p-value = 0.020), as shown in the Fig.6C and D, suggesting that blood to CSF barrier mediated delivery of arterial blood water from the ChP into ventricular CSF is directly proportional to the ChP tissue perfusion, however, the rate of exchange is not one to one. Note also that low intensity signals in the BCSFB weighted images, as shown in the Fig.6B, were also observed in various areas of the CSF compartment including the LVs, cortical surface, and peri-vascular spaces of the basal arteries in agreement with data reported in recent study in humans, and potentially indicative of labelled blood water exchanging with CSF (Petitclerc et al., 2021). Similar to the ChP, ‘hot spots’, we also observed higher than normal ASL signals at the level of the basal arteries and the $\Delta M_{TE=150\ ms}$ within these ROIs were calculated and are plotted in the Fig.7. The signals associated with the basal arteries were ~40% (0.59 ± 0.20) of those observed in the ChP (1.44 ± 0.31) but substantially higher than the background noise level. Therefore, we concluded that the lower BCSFB weighted image intensities associated with the basal arteries were not random noise but ‘genuine’ and indicative of labelled blood water exchanging with peri-vascular CSF.

4. Discussion

The objective of this study was to quantify ChP tissue perfusion and 'arterial blood water exchange with CSF', also known as 'BCSFB' mediated water exchange using the non-invasive CASL MRI imaging technique. BCSFB-ASL is an attractive non-invasive method for studying BCSFB function as it measures the unidirectional water movement from the ChP to the CSF compartment. In our study we implemented CASL which uses a long pulse labelling duration to enhance SNR permitting acquisition of data at higher spatial resolution than previous studies in mice which used a pulsed ASL sequence (Evans et al., 2020; Perera et al., 2021). From our CASL experiments we draw the following main conclusions: (1) the ChP perfusion-weighted signals acquired at TE = 23ms comprises both ChP tissue perfusion as well as the BCSFB water flow; (2) when the CASL protocol was applied to suppress the tissue perfusion signals to near background noise (acquisitions at TE = 150ms), the BCSFB-ASL signal within the LV was spatially heterogeneous and the BCSFB-ASL 'hot spot' signals coincided with the exact locations of ChP tissue; (3) we validated the BCSFB-ASL sequence in the rat brain by confirming downregulation of ChP perfusion as well as BCSFB water flow with systemic administration of vasopressin (Evans et al., 2020; Perera et al., 2021), and (4) we observed differential effects of two anesthetic regimens on the coupling of ChP perfusion and BCSFB water flow.

We developed a novel processing approach and modelled the ChP perfusion-weighted signal taken at TE = 23ms as the sum of the partial signal contributions from ChP tissue perfusion and BCSFB water flow. While the CTX perfusion-weighted signals plotted as a function of TE adhered to a mono-exponential signal decay, the perfusion-weighted signal decay in the ChP deviated from the mono-exponential decay at later TEs, implying signal mixing between multiple compartments. Interestingly, other MRI modalities such as diffusion and T2 relaxometry studies share similar attributes that involve complex interactions between water and the macro and micro-environment of the cellular and interstitial matrix, which result in multi-exponential signal decays with respect to parameters like TEs and b-factors (Alexander et al., 2001; Does, 2018; Graham et al., 1996; Niendorf et al., 1996; Riemer et al., 2018). In this study using CASL we uncovered that the ChP perfusion-weighted signal did not follow a mono-exponential decay due to partial volume effects of ChP tissue perfusion and BCSFB water flow. Further, without correcting for the partial volume effects the ChP tissue perfusion was significantly underestimated (nearly 2- to 3-fold) underscoring the importance of considering partial volume effects when studying ChP tissue perfusion, at least in a small animal species such as rodents. However, it remains an open question whether similar partial volume effects will also impact ChP tissue perfusion measurement in humans and more studies are needed to clarify this important issue (Alisch et al., 2021; Johnson et al., 2021; Petitclerc et al., 2021; Zhao et al., 2020).

Partial volume effects in ASL have been studied extensively in human cerebral perfusion experiments and often employ computerized methods to segment each voxel into the three tissue compartments: grey matter (GM), white matter (WM) and CSF (Chappell et al., 2021; Zhao et al., 2020). Due to the lack of publicly available software and algorithms to reliably segment the ChP into distinct compartments in rodents, the present study employed T2 relaxometry which allowed us to probe distinct compartments without a priori assumptions

about the number of compartments within the ChP (Does, 2018; Graham et al., 1996; Serradas Duarte and Shemesh, 2018). Here we used the smoothed T2 distribution curves to identify the different compartments. Specifically, one compartment was observed in the CTX (unimodal peak) and two compartments in the ChP (bimodal peaks).

A single peak observed in CTX at T2 ~40ms was consistent with a previous study (de Graaf et al., 2006) and overlapped with a peak of a shorter T2 compartment within the ChP. We therefore concluded that the ChP tissue and CTX share identical T2s and that the apparent T2 in the ChP is significantly overestimated without the abovementioned partial volume effect correction (Alisch et al., 2021). The other peak noticed in the 'ChP' was characterized by a long T2 ~300ms which, we identified as CSF since no other tissue or blood compartment retains such long T2 (Daoust et al., 2017; de Graaf et al., 2006). Note that numerical Laplace transformation is known to be sensitive to noise and imposes relatively stringent requirements on experimental conditions in order to attain accurate and robust results (Does, 2018; Graham et al., 1996). Therefore, we evaluated the CONTIN algorithm using simulated bi-exponential signals with noise levels identical to our experiment. The results indicated that the derived parameters were within a 5% margin of error suggesting that our experimental conditions are sufficient to accurately derive T2 distribution curves and fractional volume calculations.

Whether or not the rate of water exchange from blood into CSF, termed BCSFB water flow, is directly related with CSF secretory function in the ChP still needs further investigation. To further validate this claim, we performed simultaneous recordings of CTX perfusion, the apparent ChP blood perfusion and BCSFB water flow using an interleaved CASL acquisition with short- and long TE CASL, and also evaluated the pharmacological effect of vasopressin, a drug known to reduce ChP blood perfusion and consequently CSF secretory function (Faraci et al., 1994; Faraci et al., 1990). Our vasopressin results are in agreement with previous studies and support the BCSFB water flow as a surrogate marker for CSF secretory function (Evans et al., 2020; Perera et al., 2021). Whether or not the origin of BCSFB water flow reflects CSF secretory function only, driven by active water transport, or represents a combination of CSF secretion and diffusive water exchange (i.e PVS-CSF signals in Fig.7) remains an open question. Notably, Evans et. al reported that the estimated total blood water into the LV was substantially higher than CSF secretion rate measured using an invasive method by Liu et. al (Liu et al., 2020).

In addition to the downregulation of BCSFB water flow by vasopressin, we also noted that the CTX perfusion progressively increased consistent with previous reports (Chung et al., 2003; Kozniewska and Szczepanska-Sadowska, 1990; Perera et al., 2021; Suzuki et al., 1993). It has been suggested that the mechanism underlying the vasopressin-induced increase in cerebral perfusion is mediated by V2 receptors or the release of nitric oxide from the endothelium (Chung et al., 2003; Suzuki et al., 1993). However, here we offer an alternative explanation. Inhalational anesthetics, like isoflurane used in relatively high concentrations (~2-2.5%), is known to partially obliterate cerebral autoregulation which under normal conditions keeps the cerebral perfusion constant and within a normal physiological range of mean arterial pressure (Gropper, 2019). We used isoflurane in the vasopressin experiments and we attribute the observed effect of vasopressin – a

vasoconstrictor elevating the blood pressure – as a consequence of ISO-induced attenuation of autoregulation and the cerebral perfusion consequently becoming dependent on arterial pressure (Chung et al., 2003; Kozniewska and Szczepanska-Sadowska, 1990). As always, care should be taken in interpreting the results of cerebral hemodynamics and BCSFB function in anesthetized animals (Perera et al., 2021).

We also tested the effect of two different anesthetics and observed that the cerebral perfusion was nearly 50% lower in the DEXM-I group compared to the ISO group and these differences appeared to be global. Dexmedetomidine is a potent and selective agonist of the alpha-2 adrenergic receptor known to induce cerebral vasoconstriction and lower CBF in mice and humans and our data are consistent with these data (Petrinovic et al., 2016; Prielipp et al., 2002; Zornow et al., 1990; Zornow et al., 1993). The effects of anesthetics on BCSFB function is of particular interest for studies of glymphatic transport because the choice of anesthesia and brain arousal state can profoundly affect solute transport but scarce data exists on the coupling between brain waste clearance and CSF secretory function (Benveniste et al., 2017; Hablitz et al., 2019; Xue et al., 2020). The choroid plexus is densely innervated by sympathetic nerve fibers and its secretory and hemodynamic functions are sensitive to sympathetic nerve stimulation or denervation (Johanson et al., 2008; Lindvall et al., 1978; Lindvall and Owman, 1981; Liu et al., 2020; Oreskovic et al., 2017). At the molecular level, known drivers for CSF secretory function in the ChP has been attributed to osmotic gradients between CSF and blood serum and AQP1 water channels (Praetorius et al., 2020). A recent study in mice using the direct CSF production measurement technique reported 33% higher CSF formation with isoflurane compared to a balanced anesthesia with an α2-adrenergic agonists such as with Ketamine-Xylazine (Liu et al., 2020). Although our data showed a ~15% reduction in BCSFB water flow with DEXM-I compared to ISO anesthesia it did not reach statistical significance. Probably the inherent noise in the BCSFB ASL data (i.e., the coefficient of variance of the BCSFB water flow is ~20~26%) along with the relatively small sample size (N=12) negatively impacted the ability to detect a genuine physiological difference across the two anesthetic's effect on BCSFB water flow. In a previous study, ISO anesthesia was reported to sustain CSF production but affecting its reabsorption (Artru, 1984a, b). In our study we documented a statistically significant coupling of ChP perfusion and BCSFB water flow but reports also vary in this regard. For example, no clear correlation between ChP blood perfusion and rate of CSF secretory function was reported during hypercapnia (Oppelt et al., 1963), or with wide variations of $PaCO_2$ and hypotension (Carey and Vela, 1974; Martins et al., 1976; Weiss and Wertman, 1978). These discrepancies are likely due to the commonly used tracer dilution method for measurement of CSF secretion, which is known to be sensitive to the experimental conditions (Ivan et al., 1971). More studies using BCSFB-ASL are needed to evaluate the sensitivity and reliability of this technique compared to existing invasive methods and possibly establish standardized protocols similar to cerebral perfusion ASL measurements (Alsop et al., 2015).

A number of limitations related to the imaging and analysis methods used in our study need to be considered. First, the manual delineation of the ChP inevitably might have introduced CSF contamination into the perfusion weighted data, and to circumvent such potential errors a voxel-wise perfusion calculation can instead be performed similar to a

recent human study (Petitclerc et al., 2021). However, increased spatial resolution would introduce more noise into the BCSFB weighted signals and other means to improve SNR in the data acquisitions should be considered (e.g., cryogenically cooled RF receiver coils (Li et al., 2021; Stanton et al., 2021). Second, the calculation of the T2 distribution curves by the CONTIN algorithm and the associated computational processing time and linewidths of the T2 distribution curves can be further improved using other fitting methods like non-negative least square algorithm (Graham et al., 1996). Third, the spatial variations of B1+ over the imaging volume in the MSME sequence resulted in imperfect refocusing with stimulated echoes thereby potentially corrupting the data (Weigel, 2015). Thus the accuracy of T2 distribution curves can be further improved by considering the B1+ inhomogeneities in a curve fitting algorithm (Serradas Duarte and Shemesh, 2018). Fourth, our model excluded the CASL signal contribution of the intravascular compartment of ChP. Although bipolar gradients were employed it may have been insufficient to completely null the vascular contribution, thereby potentially overestimating the apparent ChP blood perfusion. Therefore, a more complex three compartment model to explicitly model intravascular contribution with intercompartmental exchange may improve the accuracy of ChP tissue perfusion measurements (Gregori et al., 2013; Petitclerc et al., 2021; Wells et al., 2013). Lastly, we recognize that ASL signals from brain parenchymal perfusion might introduce a confound in estimating the apparent ChP blood perfusion ($f_{ChP\text{-}BCSFB}$). By thresholding the BCSFB weighted signals to detect the ChP “hot spots”, (as shown in the Supplementary Material 3) and the slice positioning for the ASL acquisitions was carefully adjusted to make sure that the imaging slice covered a ChP dense region (as shown in the Supplementary Material 1), the inclusion of some parenchyma tissue was thereby minimized when estimating $f_{ChP\text{-}BCSFB}$.

Supplementary Material

Refer to Web version on PubMed Central for supplementary material.

Acknowledgments

The author(s) disclosed receipt of the following financial support for the research, authorship, and/or publication of this article: The present work was supported by National Institutes of Health R01AT011419 (H.B.), Foundation Leducq Transatlantic Network of Excellence (16/CVD/05) (H.B.) and PureTech Health (H.B.).

The authors thank Peter Brown and Terence Nixon of MRRC (Magnetic Resonance Research Center) at Yale University for coil development and support.

Data availability statement

Imaging data and analysis software for the present study are available through reasonable request to the corresponding author.

Bibliography

Alexander AL, Hasan KM, Lazar M, Tsuruda JS, Parker DL, 2001. Analysis of partial volume effects in diffusion-tensor MRI. Magn Reson Med 45, 770–780. [PubMed: 11323803]

Alisch JSR, Kiely M, Triebswetter C, Alsameen MH, Gong Z, Khattar N, Egan JM, Bouhrara M, 2021. Characterization of Age-Related Differences in the Human Choroid Plexus Volume,

Microstructural Integrity, and Blood Perfusion Using Multiparameter Magnetic Resonance Imaging. Front Aging Neurosci 13, 734992. [PubMed: 34603011]

Alsop DC, Detre JA, Golay X, Gunther M, Hendrikse J, Hernandez-Garcia L, Lu H, MacIntosh BJ, Parkes LM, Smits M, van Osch MJ, Wang DJ, Wong EC, Zaharchuk G, 2015. Recommended implementation of arterial spin-labeled perfusion MRI for clinical applications: A consensus of the ISMRM perfusion study group and the European consortium for ASL in dementia. Magn Reson Med 73, 102–116. [PubMed: 24715426]

Artru AA, 1984a. Effects of enflurane and isoflurane on resistance to reabsorption of cerebrospinal fluid in dogs. Anesthesiology 61, 529–533. [PubMed: 6496990]

Artru AA, 1984b. Isoflurane does not increase the rate of CSF production in the dog. Anesthesiology 60, 193–197. [PubMed: 6696252]

Asllani I, Borogovac A, Brown TR, 2008. Regression algorithm correcting for partial volume effects in arterial spin labeling MRI. Magn Reson Med 60, 1362–1371. [PubMed: 18828149]

Benveniste H, Elkin R, Heerdt PM, Koundal S, Xue Y, Lee H, Wardlaw J, Tannenbaum A, 2020. The glymphatic system and its role in cerebral homeostasis. J Appl Physiol (1985) 129, 1330–1340. [PubMed: 33002383]

Benveniste H, Lee H, Ding F, Sun Q, Al-Bizri E, Makaryus R, Probst S, Nedergaard M, Stein EA, Lu H, 2017. Anesthesia with Dexmedetomidine and Low-dose Isoflurane Increases Solute Transport via the Glymphatic Pathway in Rat Brain When Compared with High-dose Isoflurane. Anesthesiology 127, 976–988. [PubMed: 28938276]

Benveniste H, Liu X, Koundal S, Sanggaard S, Lee H, Wardlaw J, 2019. The Glymphatic System and Waste Clearance with Brain Aging: A Review. Gerontology 65, 106–119. [PubMed: 29996134]

Bolinger L, Prammer M, Leigh J, 1989. A multiple-frequency coil with a highly uniform B1 field. Journal of Magnetic Resonance 81.

Brinton RE, Gee KW, Wamsley JK, Davis TP, Yamamura HI, 1984. Regional distribution of putative vasopressin receptors in rat brain and pituitary by quantitative autoradiography. Proc Natl Acad Sci U S A 81, 7248–7252. [PubMed: 6095279]

Buxton RB, Frank LR, Wong EC, Siewert B, Warach S, Edelman RR, 1998. A general kinetic model for quantitative perfusion imaging with arterial spin labeling. Magn Reson Med 40, 383–396. [PubMed: 9727941]

Cada A, de la Torre JC, Gonzalez-Lima F, 2000. Chronic cerebrovascular ischemia in aged rats: effects on brain metabolic capacity and behavior. Neurobiol Aging 21, 225–233. [PubMed: 10867207]

Carey ME, Vela AR, 1974. Effect of systemic arterial hypotension on the rate of cerebrospinal fluid formation in dogs. J Neurosurg 41, 350–355. [PubMed: 4413096]

Chappell M, MacIntosh B, Okell T, 2018. Introduction to perfusion quantification using arterial spin labelling. Oxford University Press, Oxford.

Chappell MA, McConnell FAK, Golay X, Gunther M, Hernandez-Tamames JA, van Osch MJ, Asllani I, 2021. Partial volume correction in arterial spin labeling perfusion MRI: A method to disentangle anatomy from physiology or an analysis step too far? Neuroimage 238, 118236. [PubMed: 34091034]

Chung C, Vaquero J, Gottstein J, Blei AT, 2003. Vasopressin accelerates experimental ammonia-induced brain edema in rats after portacaval anastomosis. J Hepatol 39, 193–199. [PubMed: 12873815]

Daoust A, Dodd S, Nair G, Bouraoud N, Jacobson S, Walbridge S, Reich DS, Koretsky A, 2017. Transverse relaxation of cerebrospinal fluid depends on glucose concentration. Magn Reson Imaging 44, 72–81. [PubMed: 28782676]

de Graaf RA, Brown PB, McIntyre S, Nixon TW, Behar KL, Rothman DL, 2006. High magnetic field water and metabolite proton T1 and T2 relaxation in rat brain in vivo. Magn Reson Med 56, 386–394. [PubMed: 16767752]

De Jong GI, Farkas E, Stienstra CM, Plass JR, Keijser JN, de la Torre JC, Luiten PG, 1999. Cerebral hypoperfusion yields capillary damage in the hippocampal CA1 area that correlates with spatial memory impairment. Neuroscience 91, 203–210. [PubMed: 10336071]

Dobre MC, Ugurbil K, Marjanska M, 2007. Determination of blood longitudinal relaxation time (T1) at high magnetic field strengths. Magn Reson Imaging 25, 733–735. [PubMed: 17540286]

Does MD, 2018. Inferring brain tissue composition and microstructure via MR relaxometry. Neuroimage 182, 136–148. [PubMed: 29305163]

Evans PG, Sokolska M, Alves A, Harrison IF, Ohene Y, Nahavandi P, Ismail O, Miranda E, Lythgoe MF, Thomas DL, Wells JA, 2020. Non-Invasive MRI of Blood-Cerebrospinal Fluid Barrier Function. Nat Commun 11, 2081. [PubMed: 32350278]

Faraci FM, Kinzenbaw D, Heistad DD, 1994. Effect of endogenous vasopressin on blood flow to choroid plexus during hypoxia and intracranial hypertension. Am J Physiol 266, H393–398. [PubMed: 8141339]

Faraci FM, Mayhan WG, Farrell WJ, Heistad DD, 1988. Humoral regulation of blood flow to choroid plexus: role of arginine vasopressin. Circ Res 63, 373–379. [PubMed: 3396158]

Faraci FM, Mayhan WG, Heistad DD, 1990. Effect of vasopressin on production of cerebrospinal fluid: possible role of vasopressin (V1)-receptors. Am J Physiol 258, R94–98. [PubMed: 2137302]

Fernandez N, Martinez MA, Garcia-Villalon AL, Monge L, Dieguez G, 2001. Cerebral vasoconstriction produced by vasopressin in conscious goats: role of vasopressin V(1) and V(2) receptors and nitric oxide. Br J Pharmacol 132, 1837–1844. [PubMed: 11309256]

Firbank MJ, Coulthard A, Harrison RM, Williams ED, 1999. A comparison of two methods for measuring the signal to noise ratio on MR images. Phys Med Biol 44, N261–264. [PubMed: 10616158]

Grade M, Hernandez Tamames JA, Pizzini FB, Achten E, Golay X, Smits M, 2015. A neuroradiologist's guide to arterial spin labeling MRI in clinical practice. Neuroradiology 57, 1181–1202. [PubMed: 26351201]

Graham SJ, Stanchev PL, Bronskill MJ, 1996. Criteria for analysis of multicomponent tissue T2 relaxation data. Magn Reson Med 35, 370–378. [PubMed: 8699949]

Gregori J, Schuff N, Kern R, Gunther M, 2013. T2-based arterial spin labeling measurements of blood to tissue water transfer in human brain. J Magn Reson Imaging 37, 332–342. [PubMed: 23019041]

Gropper MA, 2019. Miller's anesthesia, 9th. ed. Elsevier, Philadelphia.

Hablitz LM, Vinitsky HS, Sun Q, Staeger FF, Sigurdsson B, Mortensen KN, Lilius TO, Nedergaard M, 2019. Increased glymphatic influx is correlated with high EEG delta power and low heart rate in mice under anesthesia. Sci Adv 5, eaav5447. [PubMed: 30820460]

Heisey SR, Held D, Pappenheimer JR, 1962. Bulk flow and diffusion in the cerebrospinal fluid system of the goat. Am J Physiol 203, 775–781. [PubMed: 13953498]

Herscovitch P, Raichle ME, 1985. What is the correct value for the brain--blood partition coefficient for water? J Cereb Blood Flow Metab 5, 65–69. [PubMed: 3871783]

Hirschler L, Collomb N, Voiron J, Kohler S, Barbier EL, Warnking JM, 2020. SAR comparison between CASL and pCASL at high magnetic field and evaluation of the benefit of a dedicated labeling coil. Magn Reson Med 83, 254–261. [PubMed: 31429990]

Ho ML, 2018. Arterial spin labeling: Clinical applications. J Neuroradiol 45, 276–289. [PubMed: 30016705]

Iliff JJ, Wang M, Liao Y, Plogg BA, Peng W, Gundersen GA, Benveniste H, Vates GE, Deane R, Goldman SA, Nagelhus EA, Nedergaard M, 2012. A paravascular pathway facilitates CSF flow through the brain parenchyma and the clearance of interstitial solutes, including amyloid beta. Sci Transl Med 4, 147ra111.

Iturria-Medina Y, Sotero RC, Toussaint PJ, Mateos-Perez JM, Evans AC, Alzheimer's Disease Neuroimaging, I, 2016. Early role of vascular dysregulation on late-onset Alzheimer's disease based on multifactorial data-driven analysis. Nat Commun 7, 11934. [PubMed: 27327500]

Ivan A, Dumitrascu E, Brinzei E, Duda R, Vancea G, Rozen M, 1971. [Epidemiological and statistico-mathematical observations on some relations between influenzal infection and evolution of pregnancy]. Rev Med Chir Soc Med Nat Iasi 75, 669–676. [PubMed: 5165046]

Jessen NA, Munk AS, Lundgaard I, Nedergaard M, 2015. The Glymphatic System: A Beginner’s Guide. Neurochem Res 40, 2583–2599. [PubMed: 25947369]

Johanson CE, Duncan JA 3rd, Klinge PM, Brinker T, Stopa EG, Silverberg GD, 2008. Multiplicity of cerebrospinal fluid functions: New challenges in health and disease. Cerebrospinal Fluid Res 5, 10. [PubMed: 18479516]

Johnson SE, McKnight CD, Jordan LC, Claassen DO, Waddle S, Lee C, Garza M, Patel NJ, Davis LT, Pruthi S, Trujillo P, Chitale R, Fusco M, Donahue MJ, 2021. Choroid plexus perfusion in sickle cell disease and moyamoya vasculopathy: Implications for glymphatic flow. J Cereb Blood Flow Metab 41, 2699–2711. [PubMed: 33906512]

Karimy JK, Kahle KT, Kurland DB, Yu E, Gerzanich V, Simard JM, 2015. A novel method to study cerebrospinal fluid dynamics in rats. J Neurosci Methods 241, 78–84. [PubMed: 25554415]

Karimy JK, Zhang J, Kurland DB, Theriault BC, Duran D, Stokum JA, Furey CG, Zhou X, Mansuri MS, Montejo J, Vera A, DiLuna ML, Delpire E, Alper SL, Gunel M, Gerzanich V, Medzhitov R, Simard JM, Kahle KT, 2017. Inflammation-dependent cerebrospinal fluid hypersecretion by the choroid plexus epithelium in posthemorrhagic hydrocephalus. Nat Med 23, 997–1003. [PubMed: 28692063]

Kozniewska E, Szczepanska-Sadowska E, 1990. V2-like receptors mediate cerebral blood flow increase following vasopressin administration in rats. J Cardiovasc Pharmacol 15, 579–585. [PubMed: 1691387]

Kroeker R, Henkelman M, 1986. Analysis of biological NMR relaxation data with continuous distributions of relaxation times. Journal of Magnetic Resonance 69, 218–235.

Larkin JR, Simard MA, Khrapitchev AA, Meakin JA, Okell TW, Craig M, Ray KJ, Jezzard P, Chappell MA, Sibson NR, 2019. Quantitative blood flow measurement in rat brain with multiphase arterial spin labelling magnetic resonance imaging. J Cereb Blood Flow Metab 39, 1557–1569. [PubMed: 29498562]

Lee H, Mortensen K, Sanggaard S, Koch P, Brunner H, Quistorff B, Nedergaard M, Benveniste H, 2018. Quantitative Gd-DOTA uptake from cerebrospinal fluid into rat brain using 3D VFA-SPGR at 9.4T. Magn Reson Med 79, 1568–1578. [PubMed: 28627037]

Li AM, Chen L, Liu H, Li Y, Duan W, Xu J, 2021. Age-dependent cerebrospinal fluid-tissue water exchange detected by magnetization transfer indirect spin labeling MRI. Magn Reson Med.

Lindvall M, Edvinsson L, Owman C, 1978. Sympathetic nervous control of cerebrospinal fluid production from the choroid plexus. Science 201, 176–178. [PubMed: 663649]

Lindvall M, Owman C, 1981. Autonomic nerves in the mammalian choroid plexus and their influence on the formation of cerebrospinal fluid. J Cereb Blood Flow Metab 1, 245–266. [PubMed: 6276421]

Liu G, Mestre H, Sweeney AM, Sun Q, Weikop P, Du T, Nedergaard M, 2020. Direct Measurement of Cerebrospinal Fluid Production in Mice. Cell Rep 33, 108524. [PubMed: 33357428]

Louveau A, Plog BA, Antila S, Alitalo K, Nedergaard M, Kipnis J, 2017. Understanding the functions and relationships of the glymphatic system and meningeal lymphatics. J Clin Invest 127, 3210–3219. [PubMed: 28862640]

Marino I, 2021. rilt (https://www.mathworks.com/matlabcentral/fileexchange/6523-rilt). MATLAB Central File Exchange.

Martins AN, Doyle TF, Newby N, 1976. PCO(2) and rate of formation of cerebrospinal fluid in the monkey. Am J Physiol 231, 127–131. [PubMed: 961850]

Niendorf T, Dijkhuizen RM, Norris DG, van Lookeren Campagne M, Nicolay K, 1996. Biexponential diffusion attenuation in various states of brain tissue: implications for diffusion-weighted imaging. Magn Reson Med 36, 847–857. [PubMed: 8946350]

Oppelt WW, Maren TH, Owens ES, Rall DP, 1963. Effects of Acid-Base Alterations on Cerebrospinal Fluid Production. Proc Soc Exp Biol Med 114, 86–89. [PubMed: 14076922]

Oreskovic D, Rados M, Klarica M, 2017. Role of choroid plexus in cerebrospinal fluid hydrodynamics. Neuroscience 354, 69–87. [PubMed: 28456718]

Ozturk BO, Monte B, Koundal S, Dai F, Benveniste H, Lee H, 2021. Disparate volumetric fluid shifts across cerebral tissue compartments with two different anesthetics. Fluids Barriers CNS 18, 1. [PubMed: 33407650]

Parkes LM, Rashid W, Chard DT, Tofts PS, 2004. Normal cerebral perfusion measurements using arterial spin labeling: reproducibility, stability, and age and gender effects. Magn Reson Med 51, 736–743. [PubMed: 15065246]

Perera C, Harrison IF, Lythgoe MF, Thomas DL, Wells JA, 2021. Pharmacological MRI with Simultaneous Measurement of Cerebral Perfusion and Blood-Cerebrospinal Fluid Barrier Function

using Interleaved Echo-Time Arterial Spin Labelling. Neuroimage 238, 118270. [PubMed: 34144160]

Petitclerc L, Hirschler L, Wells JA, Thomas DL, van Walderveen MAA, van Buchem MA, van Osch MJP, 2021. Ultra-long-TE arterial spin labeling reveals rapid and brain-wide blood-to-CSF water transport in humans. Neuroimage 245, 118755. [PubMed: 34826596]

Petrinovic MM, Hankov G, Schroeter A, Bruns A, Rudin M, von Kienlin M, Kunnecke B, Mueggler T, 2016. A novel anesthesia regime enables neurofunctional studies and imaging genetics across mouse strains. Sci Rep 6, 24523. [PubMed: 27080031]

Phillips PA, Abrahams JM, Kelly J, Paxinos G, Grzonka Z, Mendelsohn FA, Johnston CI, 1988. Localization of vasopressin binding sites in rat brain by in vitro autoradiography using a radioiodinated V1 receptor antagonist. Neuroscience 27, 749–761. [PubMed: 3252172]

Plog BA, Lou N, Pierre CA, Cove A, Kenney HM, Hitomi E, Kang H, Iliff JJ, Zeppenfeld DM, Nedergaard M, Vates GE, 2019. When the air hits your brain: decreased arterial pulsatility after craniectomy leading to impaired glymphatic flow. J Neurosurg, 1–14.

Praetorius J, Blazer-Yost B, Damkier H, 2020. Role of the Choroid Plexus in Health and Disease. Springer.

Prasloski T, Madler B, Xiang QS, MacKay A, Jones C, 2012. Applications of stimulated echo correction to multicomponent T2 analysis. Magn Reson Med 67, 1803–1814. [PubMed: 22012743]

Prielipp RC, Wall MH, Tobin JR, Groban L, Cannon MA, Fahey FH, Gage HD, Stump DA, James RL, Bennett J, Butterworth J, 2002. Dexmedetomidine-induced sedation in volunteers decreases regional and global cerebral blood flow. Anesth Analg 95, 1052–1059, table of contents. [PubMed: 12351293]

Provencher S, 1982a. A constrained regularization method for inverting data represented by linear algebraic or integral equations. Computer Physics Communications 27, 213–227.

Provencher S, 1982b. CONTIN: A general purpose constrained regularization program for inverting noisy linear algebraic and integral equations. Computer Physics Communications 27, 229.

Riemer F, Solanky BS, Wheeler-Kingshott CAM, Golay X, 2018. Bi-exponential (23) Na T2 * component analysis in the human brain. NMR Biomed 31, e3899. [PubMed: 29480533]

Serradas Duarte T, Shemesh N, 2018. Two-dimensional magnetization-transfer - CPMG MRI reveals tract-specific signatures in fixed rat spinal cord. J Magn Reson 297, 124–137. [PubMed: 30388701]

Stanton EH, Persson NDA, Gomolka RS, Lilius T, Sigurethsson B, Lee H, Xavier ALR, Benveniste H, Nedergaard M, Mori Y, 2021. Mapping of CSF transport using high spatiotemporal resolution dynamic contrast-enhanced MRI in mice: Effect of anesthesia. Magn Reson Med 85, 3326–3342. [PubMed: 33426699]

Stollberger R, Wach P, 1996. Imaging of the active B1 field in vivo. Magn Reson Med 35, 246–251. [PubMed: 8622590]

Suzuki Y, Satoh S, Oyama H, Takayasu M, Shibuya M, 1993. Regional differences in the vasodilator response to vasopressin in canine cerebral arteries in vivo. Stroke 24, 1049–1053; discussion 1053-1044. [PubMed: 7686696]

Tarasoff-Conway JM, Carare RO, Osorio RS, Glodzik L, Butler T, Fieremans E, Axel L, Rusinek H, Nicholson C, Zlokovic BV, Frangione B, Blennow K, Menard J, Zetterberg H, Wisniewski T, de Leon MJ, 2015. Clearance systems in the brain-implications for Alzheimer disease. Nat Rev Neurol 11, 457–470. [PubMed: 26195256]

Telischak NA, Detre JA, Zaharchuk G, 2015. Arterial spin labeling MRI: clinical applications in the brain. J Magn Reson Imaging 41, 1165–1180. [PubMed: 25236477]

Thomas DL, Lythgoe MF, van der Weerd L, Ordidge RJ, Gadian DG, 2006. Regional variation of cerebral blood flow and arterial transit time in the normal and hypoperfused rat brain measured using continuous arterial spin labeling MRI. J Cereb Blood Flow Metab 26, 274–282. [PubMed: 16034369]

Vakili A, Kataoka H, Plesnila N, 2005. Role of arginine vasopressin V1 and V2 receptors for brain damage after transient focal cerebral ischemia. J Cereb Blood Flow Metab 25, 1012–1019. [PubMed: 15744246]

Wardlaw JM, Benveniste H, Nedergaard M, Zlokovic BV, Mestre H, Lee H, Doubal FN, Brown R, Ramirez J, MacIntosh BJ, Tannenbaum A, Ballerini L, Rungta RL, Boido D, Sweeney M, Montagne A, Charpak S, Joutel A, Smith KJ, Black SE, colleagues from the Fondation Leducq Transatlantic Network of Excellence on the Role of the Perivascular Space in Cerebral Small Vessel, D., 2020. Perivascular spaces in the brain: anatomy, physiology and pathology. Nat Rev Neurol 16, 137–153. [PubMed: 32094487]

Wegener S, Wu WC, Perthen JE, Wong EC, 2007. Quantification of rodent cerebral blood flow (CBF) in normal and high flow states using pulsed arterial spin labeling magnetic resonance imaging. J Magn Reson Imaging 26, 855–862. [PubMed: 17896389]

Weigel M, 2015. Extended phase graphs: dephasing, RF pulses, and echoes - pure and simple. J Magn Reson Imaging 41, 266–295. [PubMed: 24737382]

Weiss MH, Wertman N, 1978. Modulation of CSF production by alterations in cerebral perfusion pressure. Arch Neurol 35, 527–529. [PubMed: 666612]

Wells JA, Siow B, Lythgoe MF, Thomas DL, 2013. Measuring biexponential transverse relaxation of the ASL signal at 9.4 T to estimate arterial oxygen saturation and the time of exchange of labeled blood water into cortical brain tissue. J Cereb Blood Flow Metab 33, 215–224. [PubMed: 23168531]

Williams DS, Detre JA, Leigh JS, Koretsky AP, 1992. Magnetic resonance imaging of perfusion using spin inversion of arterial water. Proc Natl Acad Sci U S A 89, 212–216. [PubMed: 1729691]

Xue Y, Liu X, Koundal S, Constantinou S, Dai F, Santambrogio L, Lee H, Benveniste H, 2020. In vivo T1 mapping for quantifying glymphatic system transport and cervical lymph node drainage. Sci Rep 10, 14592. [PubMed: 32884041]

Zhang W, Williams DS, Koretsky AP, 1993. Measurement of rat brain perfusion by NMR using spin labeling of arterial water: in vivo determination of the degree of spin labeling. Magn Reson Med 29, 416–421. [PubMed: 8383791]

Zhao L, Taso M, Dai W, Press DZ, Alsop DC, 2020. Non-invasive measurement of choroid plexus apparent blood flow with arterial spin labeling. Fluids Barriers CNS 17, 58. [PubMed: 32962708]

Zornow MH, Fleischer JE, Scheller MS, Nakakimura K, Drummond JC, 1990. Dexmedetomidine, an alpha 2-adrenergic agonist, decreases cerebral blood flow in the isoflurane-anesthetized dog. Anesth Analg 70, 624–630. [PubMed: 1971500]

Zornow MH, Maze M, Dyck JB, Shafer SL, 1993. Dexmedetomidine decreases cerebral blood flow velocity in humans. J Cereb Blood Flow Metab 13, 350–353. [PubMed: 8094720]

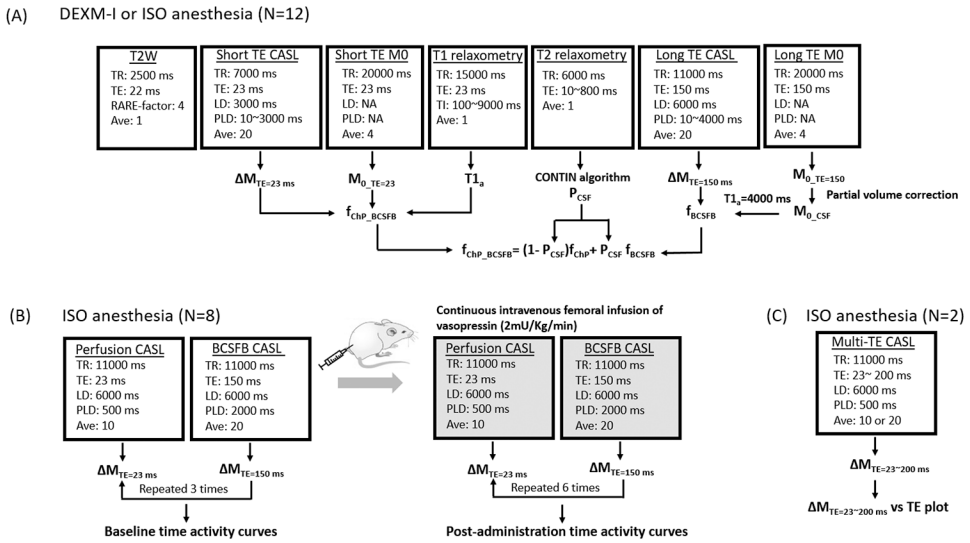

Figure 1.

Flowchart for the MR data acquisitions and analysis pipelines implemented for: (A) quantifying choroid plexus tissue blood perfusion and BCSFB water flow (B) systemic administration of vasopressin for its effects on BCSFB water flow and (C) characterization of the transverse magnetization decay of perfusion weighted signals in choroid plexus.

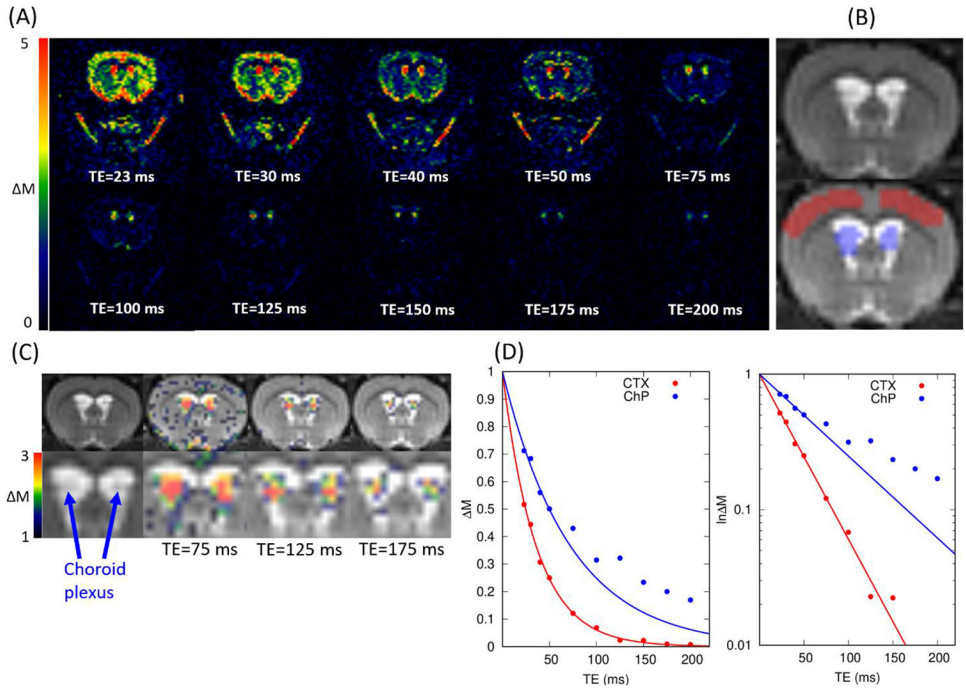

Figure 2.

(A) Representative perfusion weighted images, ΔM, in colormaps are shown as a function of echo times. Images were taken using following CASL parameters: TR = 11000ms, LD = 6000ms, and PLD = 500ms (B) T2W anatomical scan and corresponding regions of interest in cortex (red) and choroid plexus (blue). (C) Perfusion weighted images taken at TE= 75, 125 and 175ms (in color) are overlaid onto the corresponding T2W anatomical scans (in grey scale). (D) Perfusion weighted signals (N = 2) within the regions of interest are plotted as a function of echo times in cortex (red) and choroid plexus (blue). The solid lines represent the mono-exponential curve fittings using the TE = 23, 30, 40, 50ms. Both linear (left) and semi-logarithmic (right) plots are shown.

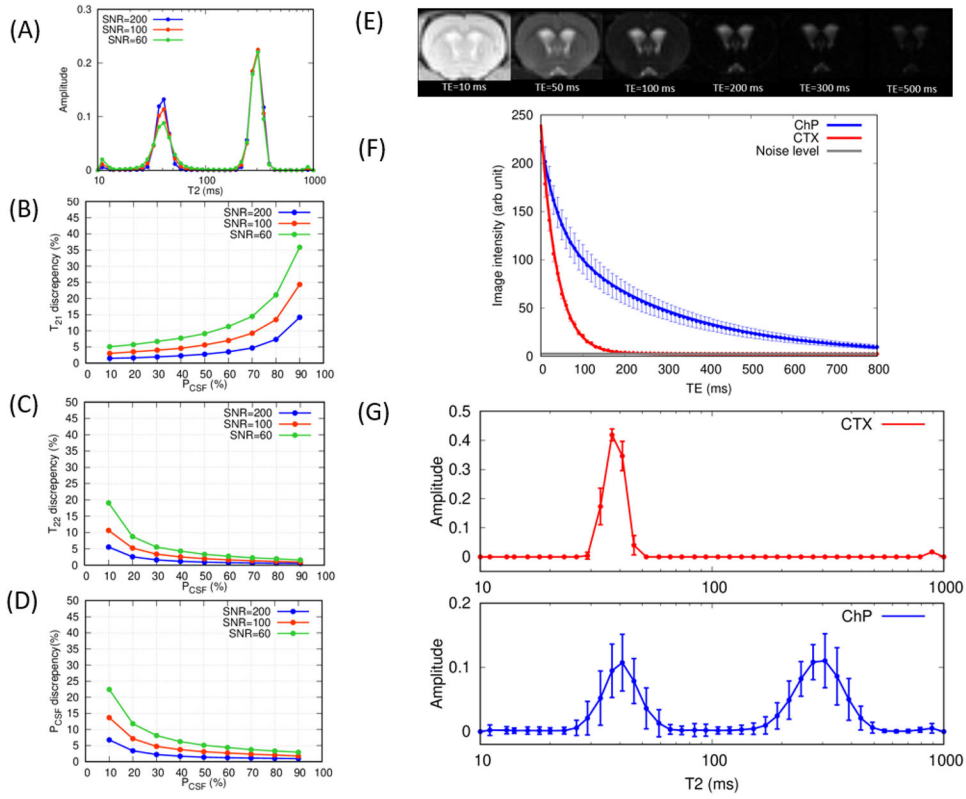

Figure 3.

(A) Averaged T2 relaxation distribution curves calculated by the CONTIN algorithm in the computer simulations when P_{CSF} = 0.6 at SNR = 60, 100, 200. (B)(C)(D) Discrepancies between the calculated and given values are plotted as a function of P_{CSF} for (B) T_{21} (C) T_{22} and (D) P_{CSF}. (E) Representative images acquired in MSME sequence at TE = 10, 50, 100, 200, 300, 500ms. (F) Population averaged (mean ± sd N=24) MSME signals are plotted as a function of echo times in cortex (red) and choroid plexus (blue). Solid lines represent the multi-compartment T2 relaxometry fits. (G) Population averaged (mean ± sd N=24) T2 relaxation distribution curves in cortex (red) and choroid plexus (blue) are shown. DEXM-I (N=12) and ISO (N=12) data were combined in the results in (F) and (G).

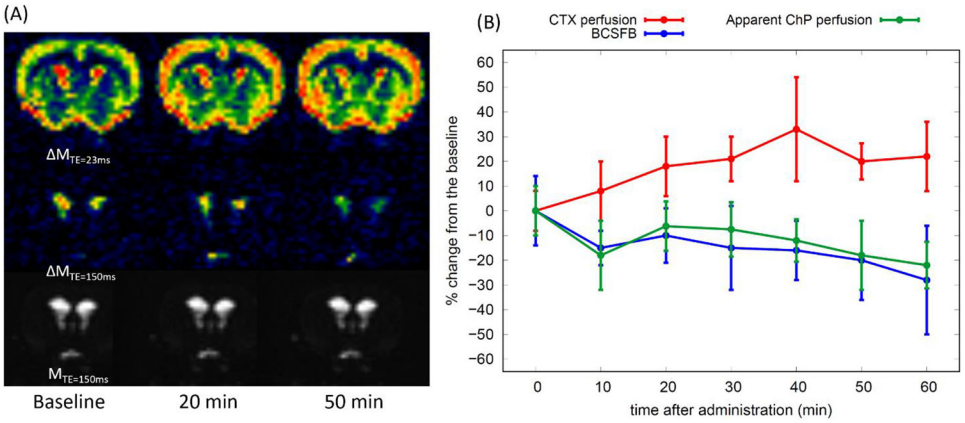

Figure 4.

(A) Representative perfusion weighted ($\Delta M_{TE=23\ ms}$), BCSFB weighted ($\Delta M_{TE=150\ ms}$), and control ($M_{TE=150ms}$) images are shown over the three time points. Images were taken at TR = 11000ms, TE = 23ms, 150ms, LD = 6000ms, PLD = 500ms. (B) % signal change (mean ± sd) between the pre (baseline) and post administration of vasopressin (N=8) are shown as a function of time.

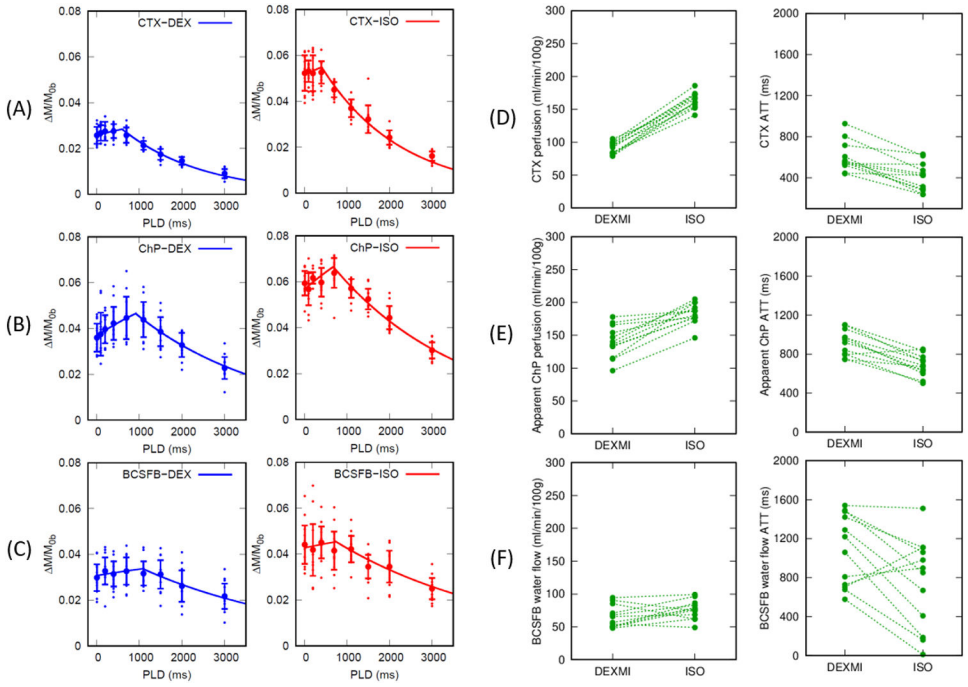

Figure 5.

(A) (B) Normalized perfusion weighted signals (mean ± sd) in cortex (CTX) and choroid plexus (ChP) are plotted as a function of PLDs in all animals (N = 12). Solid lines represent the single compartment model fits using the population averaged blood perfusion and ATT. DEXM-I (blue) and ISO (red) results are plotted. (C) Normalized BCSFB weighted signals (mean ± sd) within choroid plexus are plotted as a function of PLDs in DEXM-I (blue) and ISO (red). Solid lines represent the single compartment model fits using the population averaged BCSFB water flow and ATT. Ladder plots represent (D) CTX blood perfusion, (E) apparent ChP blood perfusion, and (F) BCSFB water flow in each animal.

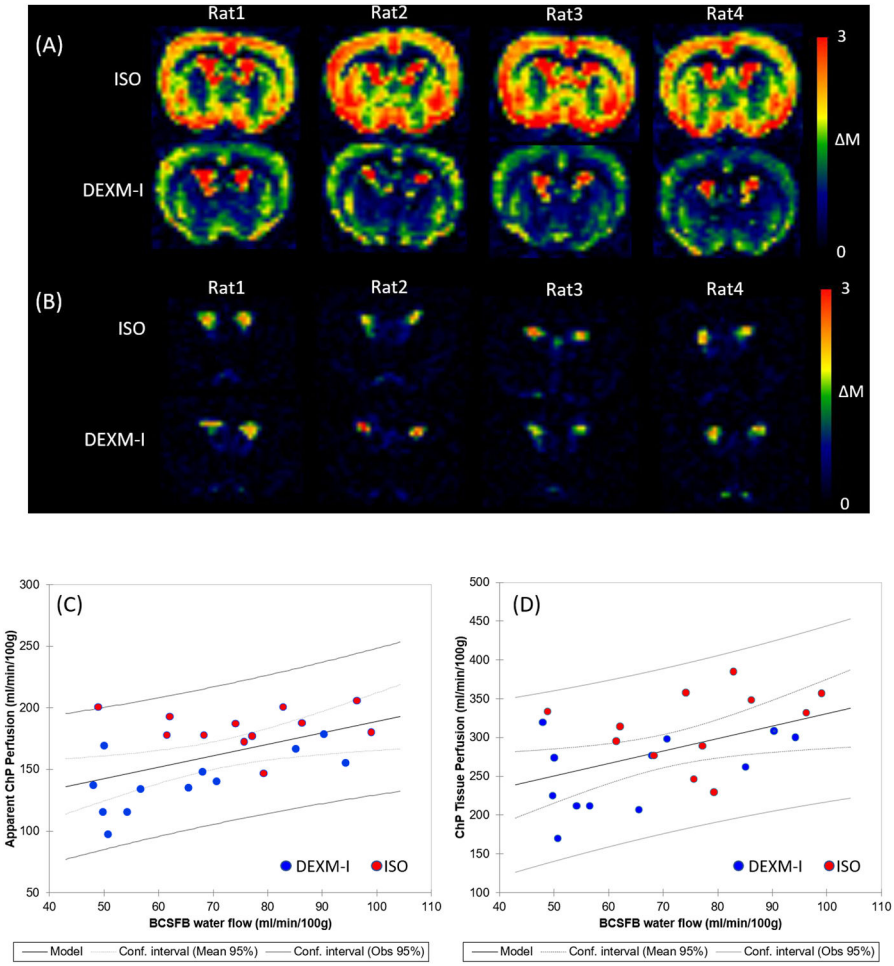

Figure 6.

(A) Perfusion weighted images ($\Delta M_{TE=23ms}$) summed over all PLDs are shown in 4 rats undergoing ISO or DEXM-I anesthesia. (B) BCSFB weighted images ($\Delta M_{TE=150ms}$) summed over all PLDs are shown in 4 rats undergoing ISO or DEXM-I anesthesia. (C) Apparent choroid plexus blood perfusion and (D) choroid plexus tissue blood perfusion are plotted as a function of BCSFB water flow. Red and blue dots represent 12 rats undergoing ISO and DEXM-I anesthesia, respectively. Solid and dotted lines represent the linear regression lines and confidence intervals, respectively.

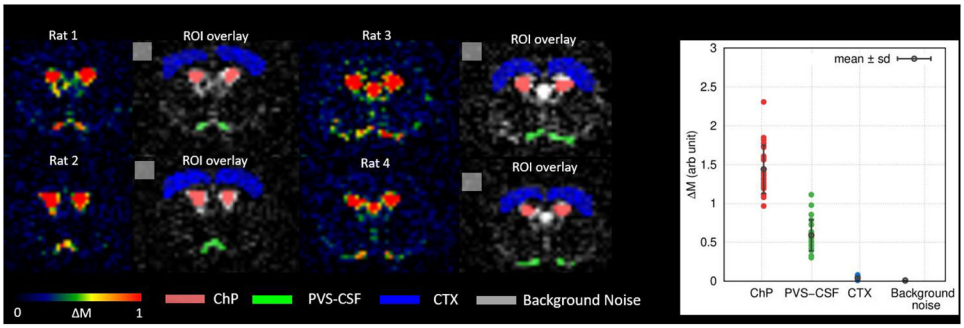

Figure 7.

(Left) Representative BCSFB weighted images ($\Delta M_{TE=150ms}$) summed over all PLDs are shown in color maps from 4 rats undergoing either ISO or DEXM-I anesthesia. Perivascular CSF associated with the basal artery (green), ChP (pink), CTX (blue), and background noise (grey) were manually delineated. (Right) DEXM-I (N=12) and ISO (N=12) data were combined and $\Delta M_{TE=150ms}$ within the regions of interest are plotted. Solid lines (black) represent the population averaged values (mean ± sd).

Table. 1

Results of blood perfusion and BCSFB water flow measurements between DEXM-I versus ISO. A summary of variables calculated in the single and multi-compartment perfusion models, multi-compartment T2 relaxometry and T1 relaxometry are given as mean ± sd. p-value is calculated by a Wilcoxon signed rank (2-sided) test. *P<0.05 is considered significant.

	DEXM-I (N=12)	ISO (N=12)	P-value
Cortical blood perfusion (ml/min/100g)	91 ± 9	164 ± 12	*0.002
ChP apparent blood perfusion (ml/min/100g)	140 ± 24	183 ± 16	*0.002
BCSFB water flow (ml/min/100g)	65 ± 17	76 ± 15	0.077
ChP tissue perfusion (ml/min/100g)	254 ± 49	313 ± 48	*0.003
Cortical blood perfusion ATT (ms)	600 ± 145	408 ± 138	*0.002
ChP apparent blood perfusion ATT (ms)	916 ± 130	680 ± 111	*0.003
BCSFB water flow ATT (ms)	1083 ± 366	746 ± 463	*0.023
CSF volume fraction in ChP (P_{CSF})	0.60 ± 0.08	0.54 ± 0.08	*0.041
Cortical T1 (ms)	1891 ± 22	1856 ± 29	*0.003
ChP T1 (ms)	3064 ± 185	3000 ± 161	0.410